Oxidation kinetics of a Ni-Cu based cermet at high temperature

Christophe Honvault, Véronique Peres, Laurent Cassayre, Pierre Chamelot, Patrice Palau, Sylvie Bouvet, Michele Pijolat

Oxidation kinetics of a Ni–Cu based cermet at high temperature

C. Honvault [a,b,c], V. Peres [a], L. Cassayre [b], P. Chamelot [b], P. Palau [c], S. Bouvet [c], M. Pijolat [a,*]

[a] Ecole Nationale Supérieure des Mines, SPIN-EMSE, CNRS:FRE3312, LPMG, 42023 Saint Etienne, France
[b] Laboratoire de Génie Chimique, UMR CNRS 5503, Université de Toulouse, 118 Route de Narbonne, F-31062 Toulouse, France
[c] Rio Tinto Alcan, Aluval 725, rue Aristide Bergès, BP 07, 38470 Voreppe, France

ARTICLE INFO

Keywords:
A. Ceramic matrix composite
A. Alloy
C. High temperature corrosion
C. Kinetic parameters
C. Internal oxidation

ABSTRACT

The oxidation kinetics of a cermet composed of Ni–Cu alloy and nickel ferrite was studied by thermogravimetry at 960 °C under oxygen in the range 0.5–77 kPa. After an initial mass increase up to 15 g/m^2 due to oxidation of surface metallic particles, the mass change was attributed to both outwards NiO growth and internal oxidation. Above 40 g/m^2, the NiO scale thickness remained constant and the oxidation kinetics followed a complete parabolic law. The variations of the kinetic rate with oxygen partial pressure allowed to propose mechanisms, rate-controlling steps and kinetic laws in both transient and long term oxidation periods.

1. Introduction

For many years, researchers in the aluminum production industry have focused on the development of environmentally friendly anode materials [1]. Indeed, since more than a century, the so-called Hall–Heroult process involves carbon anodes whose consumption produces large amounts of carbon dioxide, typically 1.5 tonnes per tonnes of aluminum. To a lesser extent, other powerful greenhouse gases such as CF_4 and C_2F_6 are also produced during anode effects [2]. Nowadays, these emissions are considered as an important environmental and economic drawback for the aluminum production industry.

Inert anode materials, which allow evolving oxygen instead of carbon dioxide, must resist to a highly corrosive environment composed of the electrolyte ($NaF–AlF_3–Al_2O_3$ based salt) and also of the surrounding oxidative gaseous atmosphere at high temperature, 900–1000 °C, without losing their conduction properties. As regularly reported by Pawlek [3–6], and detailed by Galasiu et al. [7], many materials (metals, ceramics and ceramic–metal composites called cermets) have been developed for this application, but up to date none of them was found resistant enough against corrosion for a long term (about 2 years) industrial application.

In this work, the oxidation behavior of a cermet composed of two ceramic phases and a dispersed metallic alloy was studied. The principle of such material, designed in the view of combining the advantages of both ceramics and metals, was patented by Eltech [8] and Alcoa [9] in the eighties. Pilot scale tests were driven, and led to unsatisfactory aluminum purity as well as insufficient mechanical properties causing a breakage of the anodes [10,11]. More recent work from Alcoa focused on optimizing the cermet composition and electrolyte chemistry [12,13] while studies from Thonstad and co-workers [14–18] and Liu et al. [19] have been dedicated to the understanding of its degradation mechanisms in the molten salt.

Studies concerning the oxidation behavior of the aerial part of anode materials are much less numerous. The high temperature oxidation of some alloys suitable for a use as inert anode has been investigated [20–22], but almost no work has been devoted to cermet materials. In a previous study [23], the oxidation behavior of a Ni–Cu alloy (56 mol% Ni) based cermet was investigated at various oxygen partial pressures. The morphological changes of the samples were rather complex, revealing the external growth of two oxide scales (copper and nickel oxides), and the simultaneous internal oxidation of the metallic particles, due to the inward penetration of oxygen via grain boundaries. The long term kinetic rate was found to increase with the oxygen partial pressure up to 5.1 kPa, whereas for higher oxygen pressures it became independent of the pressure. The value of the limiting pressure was found to correspond to the equilibrium pressure between tenorite (CuO) and cuprite (Cu_2O) phases at 960 °C.

In this article, we report a kinetic study of the oxidation at 960 °C of a cermet containing a Ni–Cu metal phase with a higher Ni content (76 mol% Ni) dispersed into a ceramic matrix based on nickel ferrite, and show the great influence of the Ni content on the oxidation behavior. The shape of the mass gain curves versus time, the sample morphology changes and the influence of the oxygen partial pressure have been investigated in order to

* Corresponding author. Tel.: +33 4 77 42 01 52; fax: +33 4 77 49 96 94.
E-mail address: mpijolat@emse.fr (M. Pijolat).

http://dx.doi.org/10.1016/j.corsci.2012.11.007

determine the mechanisms and the rate controlling step of the cermet oxidation.

2. Experimental

2.1. Starting materials

Cermet composed of nickel ferrite ($Ni_xFe_yM_{3-x-y}O_4$), and nickel-copper alloy (Ni_zCu_{1-z}) was obtained by a powder metallurgy process. Nickel based oxide ($Fe_wNi_{1-w}O$) was present as a minor phase dispersed into the ceramic matrix. The composition determined by electron probe microanalysis (EPMA; described in Section 2.3) was: $x = 0.86$, $y = 1.65$, $z = 0.76$ and $w = 0.16$. The distribution of the various phases derived from quantitative images analysis (with software: Leica Qwin) was: 70% for the ferrite, 19% for the alloy, 6% for the oxide and 5% for the porosity. M represents a cation which did not play any role in the oxidation process since during all the high temperature treatment it remained in the spinel phase with the same valence.

Fig. 1 shows the microstructure of the cermet from scanning electron microscopy image of backscattered electrons (BSE). The metallic alloy particles (due to their high backscattering coefficient the metal particles appear more brilliant than the other phases) present an irregular shape with an equivalent diameter of about 5 μm (a), and they are surrounded by the continuous ferrite phase (b). The nickel oxide (c) appears in various parts of the ceramic matrix as small areas (less than 5 μm) surrounded by the ferrite phase. The black areas correspond to the residual porosity.

Cermets were provided in the form of cylindrical bars with a diameter between 8 and 9 mm. The bars were cut to obtain thin discs of approximately 0.4 mm thickness for the thermogravimetry experiments. In this way, the weight gain due to oxidation on the cylindrical edge of the discs is at the very most 10% of the total surface of the sample, so it will impact slightly the quantities deduced from the kinetic analysis of the weight gain curves (cf. Section 4.1) since in this case, the mass gain due to the edge has to be neglected. However, as far as the ratios of kinetic rates are concerned (cf. Section 4.2), the whole surface of the sample may be considered since no geometrical assumption at all is necessary. The mass of the discs was between 130 and 150 mg.

2.2. Thermogravimetric analysis

The oxidation behavior of the cermets was monitored by thermogravimetry using a symmetrical SETARAM TGA16 thermobalance. Alumina crucibles and quartz suspensions were used. Prior to the oxidation treatment, the residual gases were evacuated by a primary pump. Then flowing helium (2 L/h) was introduced at atmospheric pressure and the temperature was raised from 20 to 960 °C (30 °C/min). At the furnace outlet, the gas contained less than 50 ppm oxygen as measured by an oxygen probe (Systech 910B). The mass gain during the temperature increase up to 960 °C was less than 10 μg which is negligible compared to the mass gain during the isothermal oxidation. Oxygen partial pressure was controlled by a flowmeter (BROOKS 5850S) in the range 0.5–77 kPa.

The oxidation experiments were performed under isobaric and isothermal conditions, the global gas flow rate remaining constant. During some experiments, sudden jumps in oxygen partial pressure were performed by changing the flowmeter setting, the time necessary to achieve the new partial pressure value did not exceed 5 min. At the end of the experiment, the temperature was decreased to room temperature at 30 °C/min.

In order to test the establishment of a steady state during oxidation, an experiment was done in isobaric and isothermal conditions using a SETARAM TGA16 thermobalance equipped with a differential scanning calorimetric (DSC) rod. The DSC sensor allows monitoring of the kinetic rate of oxidation since the heat released from the sample is proportional to the enthalpy of reaction. If both signals from the DSC sensor and from the derivative vs. time of the mass change can be superimposed, it means that no accumulation of any reacting species occurs in the various parts of the sample [24].

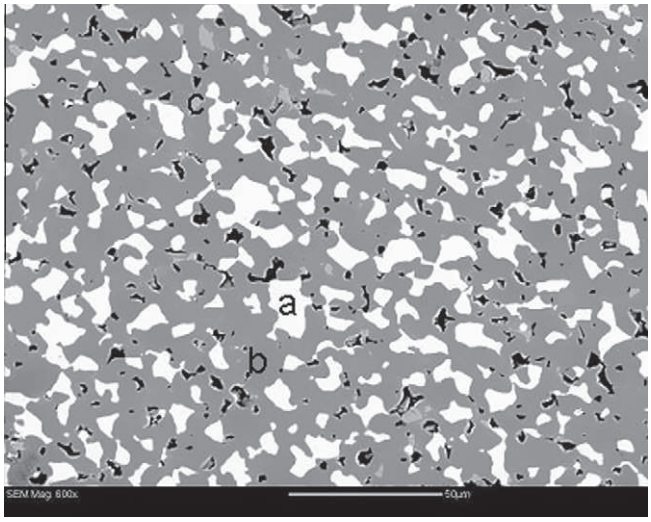

Fig. 1. Back scattered electron micrograph of the initial cermet: (a) alloy, (b) ferrite, (c) nickel oxide.

2.3. Scanning electron microscopy and electron probe microanalysis

Observations were done on samples half-cut with a diamond disc and embedded in a resin before grinding with 100 to 1200 grains/cm^2 SiC paper using water and polishing on polishing cloths with 9 to 1 μm diamond pastes. Prior to the observations, a 3 nm gold–palladium layer was sputtered on the sample with a BALZERS SCD 050 coater. Scanning electron microscopy (SEM) observations were carried out using a JEOL 6400. Quantitative electron probe microanalyses (EPMA) were done with a CAMECA SX 100.

2.4. Images analysis

Leica Qwin was used to perform image analysis on SEM micrographs to characterize the porosity. Each analysis was performed on 300 μm wide micrographs and repeated twice for each sample. Pores with diameter less than 0.1 μm were not taken into account in the quantitative treatment.

3. Results

3.1. Mass variation during oxidation at 960 °C

Fig. 2 represents the mass gain curve vs. time of a sample oxidized at 960 °C under 20 kPa of oxygen. After a fast mass increase at the very beginning of the experiment, the curve exhibits a parabolic shape which suggests diffusion controlled kinetics. The result of the DSC–TG analysis is shown in Fig. 3. The rate of mass change has been plotted vs. time of oxidation under 2 kPa of oxygen (left axis) and the scale of the DSC signal (right axis) has been adjusted in order to test if both curves can be superimposed (Fig. 3a). Both curves appear to be rather well superimposed. However, in Fig. 3b where the heat flow has been plotted as a function

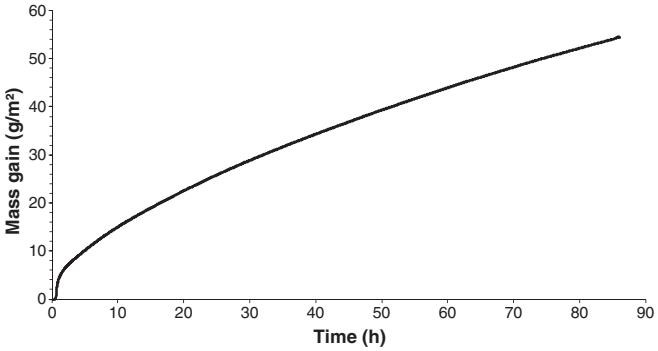

Fig. 2. Mass gain curve vs. time of oxidation at 960 °C under 20 kPa of oxygen partial pressure.

of the rate of mass gain, it clearly appears that two domains may be distinguished, which correspond to mass gain lower and higher than 15 g/m^2, each of them corresponding to steady state kinetics. Below 15 g/m^2, the mass gain rate is initially high but decreases rapidly. Above 15 g/m^2, the mass gain rate still decreases, but much more slowly. The initial period (below 15 g/m^2) may be interpreted as the oxidation of the metallic particles present at the material surface. In the following, only this second period corresponding to the oxidation behavior of the bulk material will be considered.

3.2. Microstructural changes during oxidation at 960 °C

Fig. 4 shows the backscattered electrons (BSE) micrograph of a cermet oxidized during 74 h and under 2 kPa of oxygen partial pressure. Four distinct zones can be distinguished from the bulk to the surface of the material, noted C, P, E2 and E1.

The innermost zone C, where the phase composition and distribution is the same than in the initial material, consists of the not yet oxidized part of the material.

In zone P, nearly all the metallic phase has disappeared and many voids are present. Fig. 5 displays the cumulative size distributions (in % of surface occupied as a function of the particle surface) of the voids in zones E1, P and C compared to that of the metallic particles in zone C (same as in the initial cermet) obtained from image analysis. It can be seen that the lines corresponding to the voids in zone P and to the metallic particle in zone C are very similar. The porosity in zone P is between 15% and 20%, which is similar to the metallic phase percentage in zone C. Furthermore,

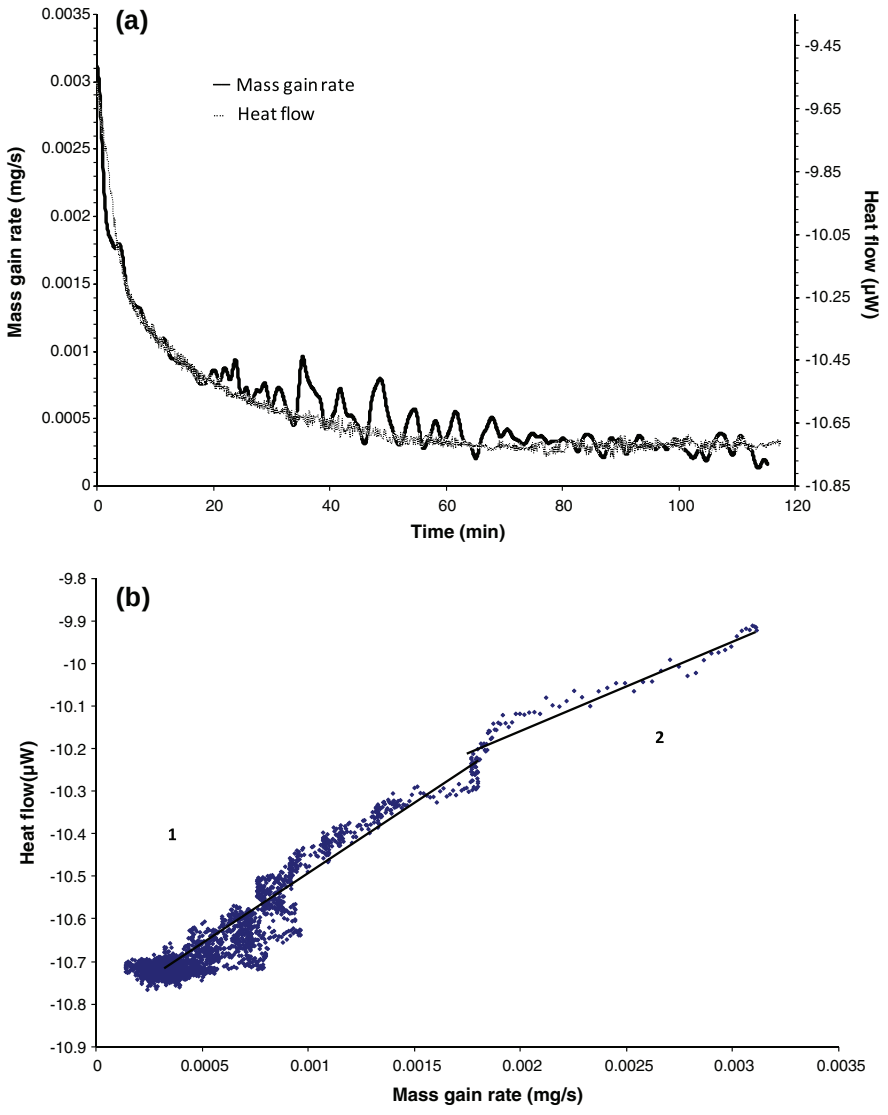

Fig. 3. Cermet oxidation at 960 °C under 2 kPa of oxygen partial pressure: (a) mass gain rate and heat flow vs. time (b) heat flow vs. mass gain rate.

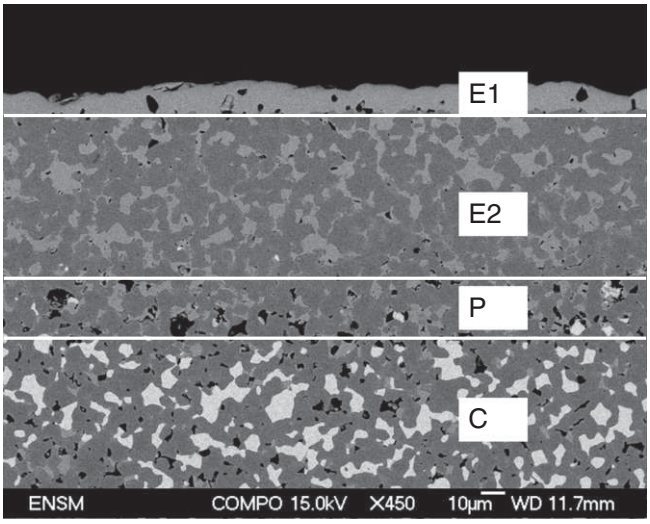

Fig. 4. Cermet after 74 h of exposure at 960 °C under 2 kPa of oxygen partial pressure.

it can be inferred that the voids in zone P correspond to the metallic particles initially present in the material. Copper and nickel cations formed at the metal/oxide interface diffuse outwards since it is well known that that the growth of copper and nickel oxides occurs by cationic transport (via cation vacancies) through the oxide layer.

Gold droplets sputtered at the surface of a cermet before oxidation showed that zone E1 corresponds to external growth of an oxide scale (Fig. 6). EPMA analysis indicated that E1 corresponds to a nickel oxide phase enriched in copper (20 mol%).

In zone E2, only two phases are present: a monoxide phase and the nickel ferrite phase. The monoxide phase is in fact, according to EPMA analysis, a solid solution of copper and nickel oxide, whose composition in copper increases gradually from the inner part to the E1/E2 interface, respectively, from 0 to 10 mol%. The composition of the nickel ferrite through the E2 layer remains nearly the same. According to the gold markers, this zone corresponds to internal oxidation.

Cermet samples were also observed after oxidation exposures at 960 °C and 20 kPa in oxygen in order to follow the variation of the thicknesses of the various zones as a function of oxidation duration. The thickness of zone P between E2 and the unreacted material (zone C) did not vary. The thicknesses of zones E1 and E2 were measured for a series of samples oxidized during various periods. Fig. 7 shows the micrographs of cermets oxidized during a: 48 h (38 g/m^2), b: 56 h (42 g/m^2), c: 70 h (48 g/m^2) and d: 86 h (54 g/m^2). On each image, it can be seen that the external layer thickness does not really change, even for the most oxidized samples (images c and d); on the less oxidized samples (a and b images) the metallic particles are still visible in zone C. In Fig. 8 have been plotted the thicknesses of the external (E1) and internal (E2) oxidation layers as a function of the total mass gain. It can be seen that the thickness of the external NiO scale increases up to 12 µm, which corresponds, for the oxidation conditions used, to a mass gain equal to 17 g/m^2 whereas the total mass gain at this moment is about 40 g/m^2; this means that in this transient period, internal and external oxide layers grow simultaneously, and after that only the internal layer keeps growing (long term period).

3.3. Oxygen partial pressure influence

To determine the oxygen partial pressure influence, the method of jumps was used in order to compare the kinetic rates measured for various pressures at the same mass gain, i.e. for exactly the same morphological state of the material (see for example Ref. [25]). The results are expressed as the variation of the ratio of the kinetic rate measured just after the jump to that measured just before the jump (denoted as "mass gain rate ratio" in the following). The samples were oxidized under 20 kPa of oxygen before the jumps. Two series of experiments were done: a first one with jumps at a mass gain equal to 24 g/m^2, and the second one with jumps at 50 g/m^2. These conditions were chosen in order to quantify separately the influence of the oxygen pressure in the transient period (in which both external and internal oxidation were found to proceed: mass gain lower than 40 g/m^2) and in the long term period (when only internal oxidation occurred: mass gain higher than 40 g/m^2). The jumps in oxygen pressure covered the range 0.5–77 kPa. Fig. 9a and b show the mass gain curves v. s. time for some experiments of both series.

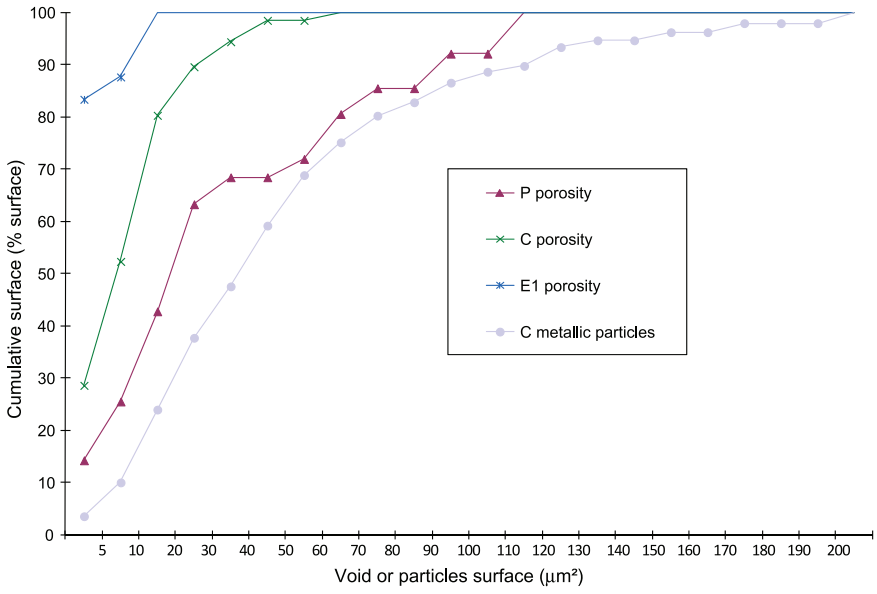

Fig. 5. Particle size distribution in porosity and metallic phases after oxidation during 60 h at 960 °C under 20 kPa of oxygen partial pressure.

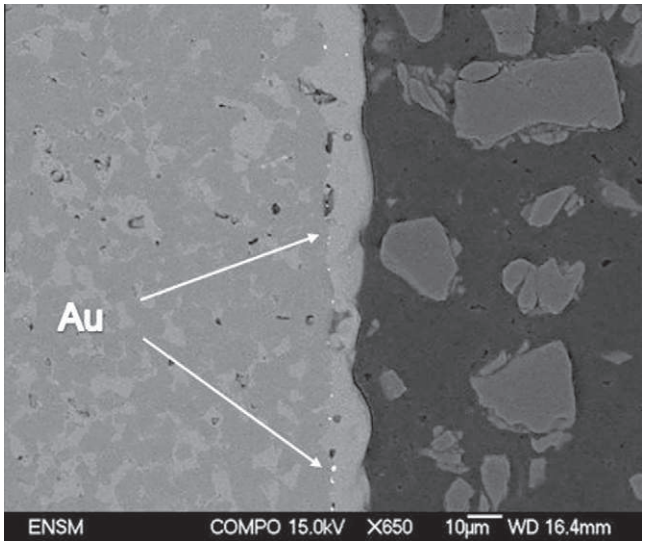

Fig. 6. Cermet after 86 h of exposure at 960 °C under 20 kPa oxygen partial pressure (gold droplets were sputtered before oxidation).

The influence of the oxygen pressure on the kinetic rate is illustrated in Fig. 10 in which the mass gain ratios have been plotted as a function of the oxygen pressure after the jump for both series. Practically, the oxidation kinetic rates were deduced from the slope of mass gain curve before and after the jumps. The relative error on the mass gain ratios was estimated from repeating three times a jump in oxygen partial pressure and measuring the deviations between the mass gain ratio values. It can be seen that there exists a difference between both series (well visible in the high pressure part of the graph) showing that the rate laws at 24 g/m^2 and at 50 g/m^2 are different. This could be expected since as previously discussed the weight gain is due in the first case to the contribution of both external and internal oxidation, and in the second case only to internal oxidation.

4. Discussion

4.1. Kinetic analysis of the mass variation during oxidation

Among the various laws used to fit the curves of the mass gain vs. time, only the complete parabolic law corresponding to Eq. (1) was found to fit the experimental curves:

$$A\Delta m^2 + B\Delta m + C = t \tag{1}$$

Fig. 11 shows the result of a fitting procedure where the time has been plotted as a function of the mass gain. The agreement between the calculated and the experimental curves is good only when a mass gain higher than 40 g/m^2 is considered.

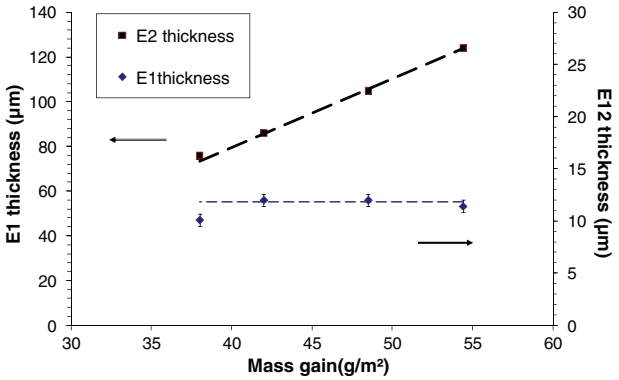

Fig. 8. External and internal oxide layer thicknesses plotted as a function of the total mass gain at 960 °C under 20 kPa of oxygen partial pressure.

Various oxidation mechanisms are accounting for a complete parabolic law: (i) oxide growth controlled by mixed diffusion and interface reactions [26,27], (ii) oxide growth controlled by diffusion with a non-protective oxide scale on top [27], and (iii) oxide growth controlled by mixed diffusion and interface reaction with a non-protective oxide scale on top [27]. The sign of *B* and *C* parameters may differ according to the oxidation mechanism. However, as presented in Section 3.2, the oxidation of the cermet involves external and internal oxidation, which disagrees with the above-mentioned mechanisms. So another explanation has to be proposed in order to well describe the oxidation behavior of the cermet.

SEM observations showed that the external oxide scale stops growing once it reaches a certain thickness. Moreover this layer appears to be dense so it must be considered as a protective layer, and diffusion across this layer must be taken into account as well as the diffusion across the inner oxide layer. Fig. 12 describes the situation of a diffusing species through layers 1 and 2 (subscripts 1 and 2) accounting for the growth of the innermost layer.

The flux across the outermost layer can be written as:

$$J_1 = -\frac{D_1}{X_1}(C_1 - C_0) \tag{2}$$

and the flux across the innermost layer:

$$J_2 = -\frac{D_2}{X_2}(C_2 - C_1) \tag{3}$$

where *X*, *D* and *C* respectively, represent the layer thickness, the diffusion coefficient and the species concentration at the various interfaces. Assuming a steady-state (and in Section 3.1. the TG-DSC experiment showed that such an assumption is valid) leads to the equality of the fluxes:

$$J_1 = J_2 \tag{4}$$

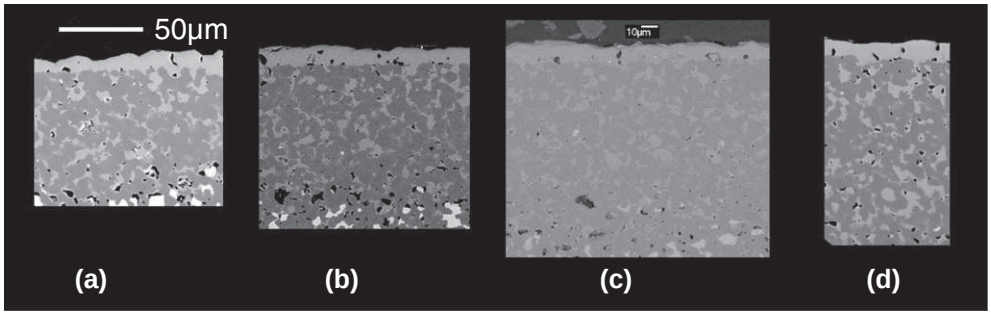

Fig. 7. Cermet oxidized under 20 kPa oxygen partial pressure at 960 °C up to (a) 38 g/m^2, (b) 42 g/m^2, (c) 48 g/m^2 and (d) 54 g/m^2.

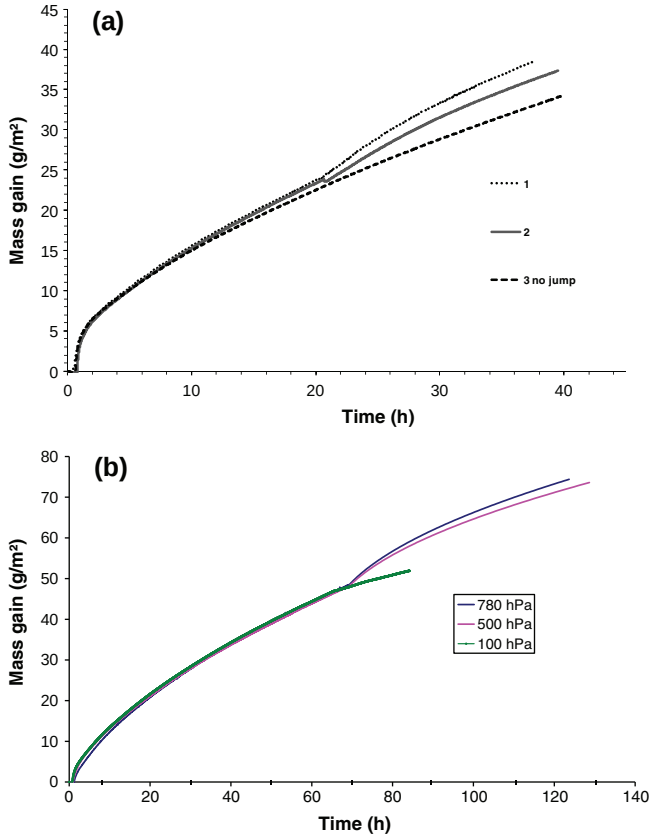

Fig. 9. Mass gain vs. time at 960 °C and under 20 kPa of oxygen partial pressure before jumps at 24 g/m^2 (a) and 50 g/m^2 (b). The values of the oxygen partial pressure after the jumps are 77 kPa (1), 50 kPa (2), 20 kPa (3), 78 kPa (4) and 10 kPa (5).

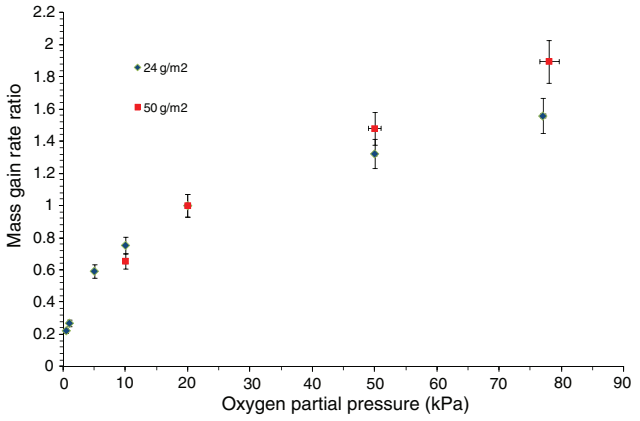

Fig. 10. Mass gain rate ratios for jumps in oxygen partial pressure vs. oxygen partial pressure after the jump for jumps done at 24 and 50 g/m^2 (oxidation at 960 °C and 20 kPa before the jumps).

Combining Eqs. (2)–(4) leads to the expression of the resulting kinetic flux J:

$$J = \frac{-D_2(C_2 - C_0)}{(X_2 + X_1) + \left(\frac{D_2}{D_1} - 1\right)X_1} \tag{5}$$

In order to obtain the rate of mass gain, the thicknesses X_1 and X_2 must be related to the corresponding mass of oxygen uptake. For the external oxide layer, if Δm_i is the mass gain between

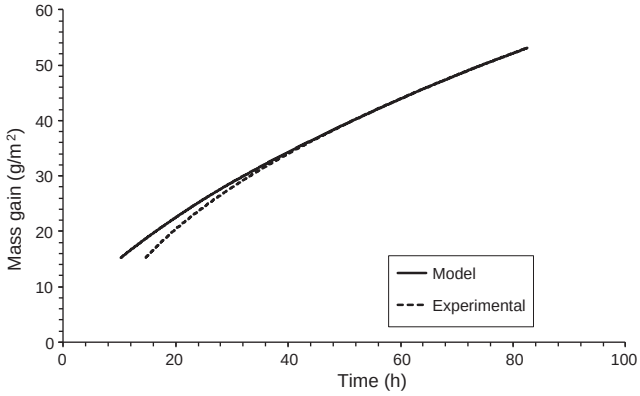

Fig. 11. Oxidation of a cermet under 20 kPa oxygen partial pressure at 960 °C: comparison between experiment and the complete parabolic law.

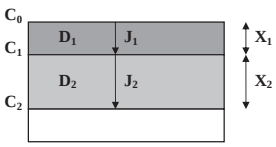

Fig. 12. Schematic view of the internal oxidation of the cermet: diffusion of a species through two successive oxide layers.

$t = 0$ and t_i, then X_1 is equal to $\Delta m_i V_m^{NiCuO}/M_O$ in the case of the inner layer, if Δm is the total mass gain at time t, X_2 is equivalent to $(\Delta m - \Delta m_i)V_m^{NiCu}/\lambda M_O$ where λ is the initial volumic fraction of metal in the cermet ($\lambda = 0.19$). Since the rate of mass gain $d(\Delta m)/dt$ is equal to the product $J\,M_O$, it comes out that:

$$\frac{d(\Delta m)}{dt} = \frac{k_p}{2\left[\Delta m + \left(\frac{D_2}{D_1}\lambda\frac{V_m^{NiCuO}}{V_m^{NiCu}} - 1\right)\Delta m_i\right]} \tag{6}$$

where:

$$k_p = 2D_2(C_0 - C_2)M_O^2\lambda/V_m^{CuNi} \tag{7}$$

Integrating Eq. (6) leads to the complete parabolic law (1) whose coefficients A, B and C take the expressions reported in Table 1.

Fitting the mass gain curves obtained at 960 °C with 20 kPa of oxygen partial pressure leads to the determination of the values of $1/A$ (i.e. k_p) and $1/B$. The mean value of k_p was found to be equal to 46 (±7) g^2 m^{-4} h^1. The value of D_2/D_1 was then of the order of 4.7 (±0.3), taking the value of Δm_i equal to 17 g m^{-2} (constant thickness of the external layer). It can thus be concluded that the internal oxidation of the cermet is controlled by mixed diffusion through the external and internal oxide layers.

4.2. Influence of the oxygen partial pressure and mechanisms

Both nickel monoxide and nickel ferrite are p-type semiconductors, their main defect are cationic vacancies (which will be noted $V_{C/Mono}$ for the cationic sites of the monoxide phase, $V'''_{C/Oct}$, $V_{C/Tet}$ for the octahedral and tetrahedral sites of the spinel ferrite phase) and

Table 1
Expression of the mass gain rate and of the complete parabolic law coefficients (cf. Eq. (1)).

Mass gain rate	A	B	C
$\frac{d\Delta m}{dt} = \frac{k_p}{2\left[\Delta m + \left(\frac{D_2}{D_1} - 1\right)\Delta m_i\right]}$	$\frac{1}{k_p}$	$\frac{2\Delta m_i}{k_p}\left(\frac{D_2}{D_1}\lambda\frac{V_m^{NiCuO}}{V_m^{NiCu}} - 1\right)$	$t_i + \frac{\Delta m_i^2}{k_p}\left(\frac{D_2}{D_1}\lambda\frac{V_m^{NiCuO}}{V_m^{NiCu}} - 1\right)^2$

electron holes (noted h° for all oxide phases) [28–30]. As mentioned in the introduction, ^{18}O atoms were evidenced at grains boundaries in a previous study by nano SIMS after oxidation of a CuNi–$NiFe_2O_4$–NiO cermet exposed to $^{18}O_2$ at 960 °C [23]; due to the similarities existing between both cermets, especially from the point of view of the internal oxidation, we suggest that oxygen diffuses along grain boundaries through the internal oxide layer to oxidize the alloy particles (E2).

Considering the external oxidation (outwards growth of nickel oxide), the most probable mechanism for the adsorption and external interface elementary steps can be written as follows:

$$O_2 + 2s \rightarrow 2O - s \tag{8}$$

$$O\text{-}s \rightarrow O_{O/Mono} + V''_{C/Mono} + s + 2h^{\circ} \tag{9}$$

where s represents an adsorption site and O-s an adsorbed oxygen atom. Since the experimental conditions are well far from equilibrium ones, a single arrow in the elementary reaction steps signifies that the kinetic rate of each step corresponds to that of the direct sense.

Considering the internal oxidation by diffusion of oxygen along grain boundaries, reaction (8) may be kept as the adsorption step, and reaction (9) may be replaced by the reaction of incorporation of the adsorbed oxygen at the surface of a grain boundary of the external oxide layer. This last step can be written as:

$$O - s \rightarrow O_{gb} + s \tag{10}$$

where O_{gb} represents an oxygen atom at a grain boundary on top of the external layer.

If one considers first the case of the internal oxidation, according to Eq. (7) the kinetic rate is proportional to k_p, i.e. to the product $D_2\,(C_0 - C_2)$. The mass action law applied to equilibria (8) and (10) (equilibrium constants noted K_1 and K_3, respectively) leads to the following expression of the concentration C_0 of the diffusing species:

$$C_0 = [O_{gb}] = K_3\sqrt{K_1 P_{O_2}} \tag{11}$$

Assuming that C_2 is negligible compared to C_0 leads to a kinetic rate proportional to the square root of the oxygen partial pressure. Fig. 13 shows the mass gain ratios obtained by the jump experiments done in the long term period of oxidation (i.e. over 40 g/m^2, only internal oxidation) as a function of the oxygen partial pressure fitted by a square root law. The agreement is quite good, which validates the proposed mechanism.

Now, concerning the preceding period of oxidation which involves both external and internal oxidation, the kinetic rate should be equal to the sum of two terms, one of them being proportional to the square root of the oxygen partial pressure (internal oxidation). If one considers the kinetic rate of growth of the external scale only (i. e. the monoxide layer), it corresponds to the classical case of the oxidation of nickel with four possible rate-limiting steps: adsorption (8), external interface reaction (9), cationic vacancy diffusion and internal interface reaction. From a theoretical point of view, it must be possible to discriminate which of these steps is rate-controlling the external layer growth by considering the influence of the oxygen pressure observed in the jumps experiments done at 24 g/m^2. The rate would be proportional to $\alpha P_{O_2}^{1/2} + \beta P_{O_2}$ in the case of adsorption (R1), to $\alpha P_{O_2}^{1/2} + \beta P_{O_2}^{1/2}/(1 + \gamma P_{O_2}^{1/2})$ in the case of the external reaction (9), to $\alpha P_{O_2}^{1/2} + \beta P_{O_2}^{1/6}$ in the case of cationic vacancy diffusion, and to $\alpha P_{O_2}^{1/2}$ in the case of the internal interface reaction. The last case may easily be discarded due to the differences observed in both series of ratios at 50 and 40 g/m^2 (cf. Fig. 9). As evidenced in Fig. 14, only the $\alpha P_{O_2}^{1/2} + \beta P_{O_2}^{1/6}$ law was found to well fit the

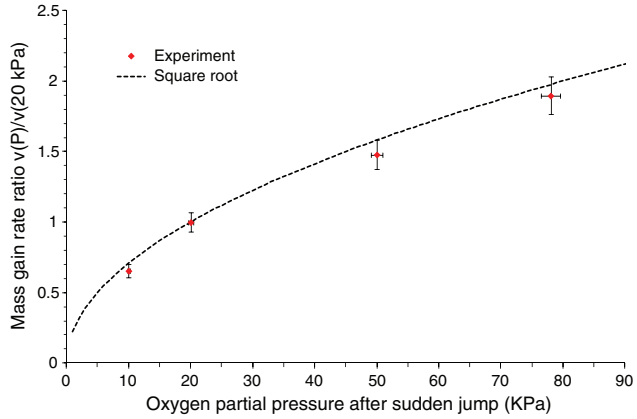

Fig. 13. Ratios of mass gain rate vs. oxygen partial pressure after sudden change at 50 g/m^2 (internal oxidation): fit to square root law.

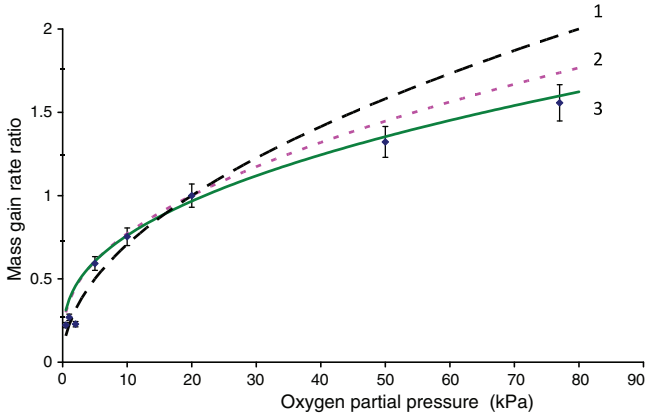

Fig. 14. Ratios of mass gain rate vs. oxygen partial pressure after sudden change at 24 g/m^2 (external and internal oxidation): fit to $\alpha P_{O_2}^{1/2} + \beta P_{O_2}$ (1), $\alpha P_{O_2}^{1/2} + \beta P_{O_2}^{1/2}/(1+\gamma P_{O_2}^{1/2})$ (2) and $\alpha P_{O_2}^{1/2} + \beta P_{O_2}^{1/6}$ (3) laws.

experimental mass gain rate ratios at 24 g/m^2. It can be added that the results are different from those previously obtained with a Cu–Ni based cermet similar to the present one, but containing less nickel in the metal phase [7]. Here, the external oxide layer is a nickel oxide phase enriched in copper, whereas in [7], it was a copper rich oxide (Cu_2O or CuO depending on the oxygen pressure). Moreover the long term kinetic behavior was nearly linear in the case of the Cu-rich cermet, which suggested an interfacial rate determining step instead of a diffusion control in the present case. The difference in the metallic phase composition, as well as the difference in the microstructure between both cermets account for the differences found on the influence of oxygen partial pressure and the rate-controlling step.

5. Conclusions

Thermogravimetry, SEM observations and the jump method allowed us to describe the kinetic behavior of a NiCu based cermet during oxidation at 960 °C under oxygen at partial pressures in the range 1–77 kPa. Both external and internal oxidations were observed. After fast oxidation of the metallic particles present at the surface of the material, two successive periods (transient and long term periods) could be distinguished from the changes of the corresponding layer thicknesses as a function of time. In the transient period, the mass gain results from the contribution of two growing oxide scales: an external NiO layer and an internal oxidized layer

corresponding to the oxidation of the metallic particles embedded in the ceramic matrix. Then the growth of the external oxide scale stops and the mass gain corresponds only to the internal oxidation (long term period). Sudden jumps in oxygen partial pressure during oxidation allowed to obtain the influence of the oxygen partial pressure on the kinetic rate. The results were consistent with a rate-limiting step of cationic vacancies diffusion through the NiO scale for the external growth, and of diffusion of oxygen species along the grain boundaries through both oxidized layers for the internal oxidation. For the long-term behavior of the cermet, it is concluded that the mass gain is obeying a complete parabolic law due to a control by oxygen diffusion along grains boundaries across both the external and the internal oxide layers.

References

[1] D.R. Sadoway, Inert anodes for the Hall–Héroult cell: the ultimate materials challenge, JOM 53 (5) (2001) 34–35.
[2] J. Thonstad, P. Fellner, G.M. Haarberg, J. Hives, H. Kvande, A. Sterten, Aluminium Electrolysis, Fundamentals of the Hall–Héroult Process, third ed., Aluminium-Verlag, Dusseldorf, 2001.
[3] R.P. Pawlek, Recent developments of inert anodes for the primary aluminium industry, Part I, Aluminium 71 (1995) 202–206.
[4] R.P. Pawlek, Recent developments of inert anodes for the primary aluminium industry, Part II, Aluminium 71 (1995) 340–342.
[5] R.P. Pawlek, Inert anodes: an update, Light Metals (2004) 283–287.
[6] R.P. Pawlek, Inert anode – an update, Aluminium 1–2 (2011) 77–81.
[7] I. Galasiu, R. Galasiu, J. Thonstad, Inert Anodes for Aluminium Electrolysis, Aluminium-Verlag, Dusseldorf, 2007.
[8] J.J. Duruz, J.P. Derivaz, Cermet anode electrowining metals from fused salts, US Patent No. 4,397,729, 1981.
[9] S.P. Ray, R.A. Rapp, Composition suitable for inert electrode, US Patent No. 4,455,211, 1984.
[10] C.F. Windisch, D.M. Strachan, C.H. Henager, T.R. Alcorn, A.T. Tabereaux, N.E. Richards, Materials characterization of cermet anodes tested in a pilot cell, Light Metals (1993) 445–454.
[11] R.D. Peterson, N.E. Richards, A.T. Tabereaux, O.H. Koski, L.G. Morgan, D.M. Strachan, Results of 100 hour electrolysis test of a cermet anode: operational results and industry perspective, Light Metals (1990) 385–401.
[12] R.A. Christini, R.K. Dawless, S.P. Ray, D.A. Weirauch, Advanced anodes and cathodes utilized in energy efficient aluminium production cells, Alcoa Technical Center, 2001.
[13] R.L. Kozareck, S.P. Ray, R.K. Dawless, A.F. LaCamera, Corrosion of cermet anodes during low temperature electrolysis of alumina, Alcoa Technical Center, 1997.
[14] E. Olsen, Nickel ferrite and tin oxide as anode materials for aluminium electrolysis, Ph.D. Thesis, NTNU, Trondheim (1995).
[15] O.A. Lorentsen, Behaviour of nickel, iron and copper by application of inert anodes in aluminium production, PhD Thesis, NTNU, Trondheim (2000).
[16] O.-A. Lorentsen, J. Thonstad, Electrolysis and post-testing of inert cermet anodes, Light Metals (2002).
[17] E. Olsen, J. Thonstad, Nickel ferrite as inert anodes in aluminium electrolysis: Part I material fabrication and preliminary testing, J. Appl. Electrochem. 29 (1999) 293–299.
[18] E. Olsen, J. Thonstad, Nickel ferrite as inert anodes in aluminium electrolysis: Part II material performance and long-term testing, J. Appl. Electrochem. 29 (1999) 301–311.
[19] J.-Y. Liu, Z.-Y. Li, Y.-Q. Tao, D. Zhang, K.-C. Zhou, Phase evolution of 17(Cu–10Ni)–($NiFe_2O_4$–10NiO) cermet inert anode during aluminium electrolysis, Trans. Nonferrous Met. Soc. China 21 (2011) 566–572.
[20] R. Haugsrud, T. Norby, P. Kofstad, High-temperature oxidation of Cu–30 wt.% Ni–15 wt.% Fe, Corros. Sci. 43 (2001) 283–299.
[21] S. Helle, M. Pedron, B. Assouli, B. Davis, D. Guay, L. Roue, Structure and high-temperature oxidation behaviour of Cu–Ni–Fe alloys prepared by high-energy ball milling for application as inert anodes in aluminium electrolysis, Corros. Sci. 52 (10) (2010) 3348–3355.
[22] V. Chapman, B.J. Welch, M. Skyllas-Kazacos, High temperature oxidation behaviour of Ni–Fe–Co anodes for aluminium electrolysis, Corros. Sci. 53 (2011) 2815–2825.
[23] F. Rioult, M. Pijolat, F. Valdivieso, M.A. Prin-Lamaze, High-temperature oxidation of a Cu–Ni based cermet: kinetic and microstructural study, J. Am. Ceram. Soc. 89 (2006) 996–1005.
[24] M. Pijolat, M. Soustelle, Experimental tests to validate the rate-limiting step assumption used in the kinetic analysis of solid-state reactions, Thermochim. Acta 478 (2008) 34–40.
[25] M. Tupin, M. Pijolat, F. Valdivieso, M. Soustelle, A. Frichet, P. Barberis, Differences in reactivity of oxide growth during the oxidation of zircaloy-4 in water vapour before and after the kinetic transition, J. Nucl. Mater. 317 (2003) 130–144.
[26] B.E. Deal, A.S. Grove, General relationship for thermal oxidation of silicon, J. Appl. Phys. 36 (1965) 3770–3778.
[27] D. Monceau, B. Pieraggi, Determination of parabolic rate constants from a local analysis of mass-gain curves, Oxid. Met. 50 (1998) 477–493.
[28] N.L. Peterson, Impurity diffusion in transition-metal oxides, Solid State Ionics 12 (1984) 201–215.
[29] K. Tsukimura, S. Sasaki, N. Kimizuka, Cation distributions in nickel ferrites, J. Appl. Phys. 36 (1997) 3609–3612.
[30] N.L. Peterson, W.K. Chen, D. Wolf, Correlation and isotope effects for cation diffusion in magnetite, J. Phys. Chem. Solids 41 (1980) 709–719.